Geochemistry, Geophysics, Geosystems

Supporting Information for

A complex mantle plume head below East Africa-Arabia shaped by the lithosphere-asthenosphere boundary topography

Chiara Civiero*[1,2], Sergei Lebedev[1,3], Nicolas L. Celli[1]

1) Dublin Institute for Advanced Studies, Geophysics Section, Dublin D02 Y006, Ireland

2) Institut de Ciències del Mar, ICM-CSIC, Passeig Marítim de la Barceloneta 37-49, 08003 Barcelona, Spain

3) Bullard Laboratories, Department of Earth Sciences, University of Cambridge, Cambridge CB30EZ, UK

Contents of this file

Figure S9. Low-velocity vote images of the whole mantle for 34 tomographic models (dv/v < 0).
Figure S10. Two proposed scenarios for the source(s) of the Afar and Levant Plumes.
Figure S11. Plume tracks at 0-60 Ma according to different plate-motion models.

Supplementary Text S1. Volcanic ages compilation

We compiled the ages of the magmatic phases for 25 volcanic areas across the East Africa-Arabia region (Fig. 2C, Supplementary Table S1). The dataset includes alkaline basaltic rocks, ranging in age from the Eocene (~45 Ma) to present. Due to the highly scattered volcanism in Anatolia and Levant, the representative ages of the basaltic samples were taken from the most significant locations of volcanic activity, i.e., the age of the largest (and generally the most discussed in literature) magmatic bodies. For simplicity, we subdivided Anatolia into three provinces, the Western Anatolia Volcanic Province (WAVP), Central Anatolia Volcanic Province (CAVP), and Eastern Anatolia Volcanic Province (EAVP). In our compilation, we used mainly the geochemical dating (e.g., $^{40}Ar/^{39}Ar$ geochronology). Supplementary Table S1 gives detailed information on data sources.

Cenozoic volcanism in Ethiopia is part of a currently active LIP, and its relative youth makes it one of the best-exposed examples in which to examine the relationships with mantle plumes. The earliest recorded volcanism started ~45–35 Ma in the southernmost Ethiopia/northern Turkana (Eocene Initial Phase, Rooney, 2017) (**22** in Fig. 2B-C and Supplementary Table S1), where a later major episode occurred 19–11 Ma (George et al., 1998). The first eruptions were followed by flood basalt activity in NE Ethiopia (**21**), Eritrea and Yemen (Oligocene Traps Phase) (**19**) at around 30 Ma (Hofmann et al., 1997; Pik et al., 1999; Rooney, 2017; Schilling et al., 1992), which erupted apparently in a short time interval (<5 Ma) and covered an area of >500,000 km^2. The origin of this event is considered to result from the interaction of the Afar mantle plume activity with the African lithosphere (Rooney, 2017). Subsequent volcanism produced a few shield volcanoes in NW Ethiopia (**21**) at 25–22 Ma (Early Eocene resurgence phase) and 11 Ma (Kieffer et al., 2004). The origin of magmatism during this event is unclear, with evidence of lithospheric melts and contributions from the Afar plume, coupled with synchronous extension of the continental crust (Rooney, 2017; Stab et al., 2016). Volcanic activity in Afar (**20**) began shortly after the eruption of the Ethiopian traps and persisted to present with discontinuous phases. The oldest volcanic formation, the Adolei basalts, erupted from 27 to 19 Ma (Deniel et al., 1994). Rhyolites on the edges of the Danakil region erupted next, between 16 and 9 Ma (Lahitte et al., 2003). This was followed by emplacement of the Dahla basaltic unit from ~8 to ~6 Ma. The largest volume of basalts in Afar, the Stratoid formation, outcrop between ~2.3 and 1 Ma, although the eruption age is still debated (Lahitte et al., 2003; Rooney, 2020). After the rift initiation ~25 Ma in Turkana, the extension propagated to the north, creating the southern Main Ethiopian Rift that merged with faults from the Afar triple junction and to the south, where it splits into the Kenya rift and the Western rift, generating episodic volcanism throughout the region. Three discrete volcanic episodes have been identified in northern Kenya (**23**): (1) prerift late Eocene-early Oligocene volcanism (32–40 Ma) in the south central portion of the Kenyan rift, (2) more voluminous synrift volcanism at 26–16 Ma in the western and eastern part of the rift, and (3) Plio-Pleistocene to present eruption of axially aligned composite volcanic centers (Furman et al., 2004, 2006). The rift opening occurred synchronously with the second pulse of volcanism. After the rift moved southward and the volcanism in the southern rift, Central Kenya (**24**) started at 15 Ma (Baker, 1986), reaching Northern Tanzania (**25**) at 5.9 Ma. Four stages of volcanic activity are identified here: the first in the ~5.9–2.9 Ma, the second between 2.6 and 1.8 Ma, the third at 1.65–0.75 Ma, and the last one starting at 0.5 Ma to present (Mana et al., 2015).

In Arabia, the first stage of volcanism—including plutons and numerous dykes that stretch along the 1,700 km of the Red Sea eastern coast—is coincident with the initiation of the opening of the Red Sea at ~30–29 Ma (Baldridge et al., 1991; Sebai et al., 1991). However, most of the volcanism is concentrated below the Arabian Shield within 100–500 km from the Red Sea, in volcanic fields locally called ‘harrats’ (**7-18**), which were active up to the Pleistocene, and in some cases up to historic times (e.g., the Madinah eruption of 1,256 AD, Camp et al. 1987).

Lava fields of both young and old ages were found from southern Arabia to Syria. Volcanism in Syria started later than in Saudi Arabia and Yemen (21 and 30 Ma, respectively, (Ershov & Nikishin, 2004; Krienitz et al., 2009)), indicating migration northwards with time (Camp et al., 1989, 1991). The volcanism in the Arabian Shield comprises two main periods: (1) the Late Oligocene to Early Miocene and (2) the Middle Miocene to Quaternary with a volcanic quiescence of several million years between the two (~20–13 Ma, Camp and Roobol 1992; Ilani et al., 2001). In Northern Syria, Miocene to Pliocene-Pleistocene volcanism and dykes erupted along the eastern flanks of the Dead Sea and several small volcanic fields aligned along the northernmost trace of the Dead Sea Transform, including the Homs (**6**) and Al Ghab (**5**) basalts (Ma et al., 2011; Weinstein & Garfunkel, 2014).

In SE Anatolia, the activity of the Karacadag volcano (**4**) lasted from ~11 Ma to ~0.1 Ma, during which a vast amount of magmas erupted to the surface, covering an area of 10,000 km^2 (Lustrino et al., 2012). Within the collisional setting of the Eastern Anatolia Volcanic Province (EAVP) (**2**), the volcanism appears to have started immediately after the rapid uplift of the East Anatolian Plateau ~11 Ma in the northern side of the plate boundary (Erzurum-Kars volcanics). After, it became widespread all over the region and migrated southward, forming large stratovolcanoes starting at 2 Ma (Keskin et al., 1998; Özdemir et al., 2006). Central Anatolia Plateau formed ~8 Ma and the uplift was preceded by the onset of widespread volcanism in the Cappadocia Volcanic Province (Central Anatolia Volcanic Province, CAVP) (**3**) between 13.5 to 8.5 Ma (Bartol & Govers, 2014). This initial activity was followed by the eruptions of ignimbrites and volcanic ash between 8.5 and 2.7 Ma. Volcanism ended with the eruption of basaltic lavas during the development of central stratovolcanoes (Dilek & Whitney, 2000). Extensive volcanism of the Western Anatolia Volcanic Province (WAVP) (**1**) developed in three distinct phases of activity (Aldanmaz et al., 2000). The oldest phase began in the Late Eocene at about 37 Ma and ended at 23 Ma in the NE part of the Biga Peninsula (Ercan et al., 1995). A second phase started in the Early-Middle Miocene (21.3–15.2 Ma), covering a broad compositional range from basalts to rhyolites. The third pulse in the Late Miocene (11.4–8.3 Ma) is characterized by alkaline rocks with OIB-like trace element patterns (11.4–8.3 Ma). Finally, during the Late Pliocene and Quaternary (~2–0 Ma), basaltic volcanism developed in the Kula region where volcanic fields are composed of several cinder and spatter cones dating back to pre-historic times (Innocenti et al., 2005).

Supplementary Text S2. Plate-motion reconstructions

We used the open-source plate-reconstruction software GPlates (www.gplates.org) following the plate polygons of Seton et al. (2012) to build the model paths, with a starting age of 60 Ma and a time interval of 10 Ma. Figure 8 and Supplementary Fig. S11 show the computed hotspot tracks that would result from the lithospheric plate moving over the Kenya, Afar, and Levant plumes for a number of alternative models, all freely available. The plate reconstruction (Torsvik et al., 2019) shown in Figure 8 uses a hybrid plate motion frame that combines hotspot and true polar wander corrected paleomagnetic reference frames, which is referred to as a mantle frame (Doubrovine et al., 2016). The other absolute plate motion (APM) models used in Supplementary Fig. S11 are: D2012 – Global moving hotspot model (Doubrovine et al., 2012); M1993 – Indo-Atlantic fixed hotspot model (Muller et al., 1993); NNR – No-Net-Rotation frame, (Argus et al., 2011); O2005 – Indo-Atlantic moving hotspot model (O'Neill et al., 2005); S2005 – Global paleomagnetic model (Schettino & Scotese, 2005); T2008 – Global moving hotspot model (Torsvik et al., 2008); T2012 – Paleomagnetic reference frame (Torsvik et al., 2012); V2010 – Slab remnant model (Van Der Meer et al., 2010); M2016 – Global model from a hybrid paleomagnetic reference frame (Torsvik et al., 2012) and hotspot tracks (Matthews et al., 2016).

The suite of different tracks gives an indication of the variability and uncertainty of the results. For example, assuming fixed hotspots, we can infer that Kenya was approximately above the Afar Plume at 60 Ma (red line in Supplementary Fig. S11). From models that take computed hotspot motion in large-scale mantle flow into account (blue line in Supplementary Fig. S11), the plume location relative to Kenya is expected somewhat further east. The tracks taken by the three upwellings to reach the surface coincide to paths of least resistance, where the lithosphere is thinner compared to the surrounding areas (see Supplementary Fig. S11B). We note that the conclusions of this study are robust and stand regardless of the choice of the plate motion reconstruction.

Supplementary Table S1

Number	Name	Magmatic phase time range (Ma)	References
1	Western Anatolia Volcanic Province (WAVP)	37-23; 21-15.2; 11.4-8.3; 2-0	Ercan et al., 1995; Aldanmaz et al., 2000; Innocenti et al., 2000
2	Eastern Anatolia Volcanic Province (EAVP)	11-6; 6-5; 5-2.7; 2.0-0	Keskin et al., 1998; 2006; Özdemir et al., 2006
3	Central Anatolia Volcanic Province (CAVP)	13.5-8.5; 8.5-2.7; 2.5-0	Le Pennac et al., 2005; Dilek and Whitney, 2000; Bartol and Govers, 2014; Di Giuseppe et al., 2018
4	Karacadag	11-2.7; 1.9-1; 0.4-0.01	Lustrino et al., 2012
5	Al Ghab	18-8; 4-1	Ma et al., 2011; Weinstein and Garfunkel, 2014; Wahab et al., 2014
6	Homs	10.1-9.8; 5.6-4	Ma et al., 2011; Weinstein and Garfunkel, 2014; Wahab et al., 2014
7	As Shaam	26-22; 13-8; 7-0.2	Weinstein and Garfunkel, 2014; Wahab et al., 2014
8	Uwayrid	9-0	Weinstein and Garfunkel, 2014; Wahab et al., 2014
9	Hutaymah	1.8-1.5	Weinstein and Garfunkel, 2014; Wahab et al., 2014
10	Ithnayn	3-0	Weinstein and Garfunkel, 2014; Wahab et al., 2014
11	Khaybar	5-0	Weinstein and Garfunkel, 2014; Wahab et al., 2014
12	Lunayyr	10-0	Weinstein and Garfunkel, 2014; Wahab et al., 2014; Duncan and Al-Amri, 2013
13	Rahat	10-0	Weinstein and Garfunkel, 2014; Wahab et al., 2014; Downs et al., 2018
14	Kishb	2-0.02	Weinstein and Garfunkel, 2014; Wahab et al., 2014

15	Hadn	28-15	Weinstein and Garfunkel, 2014; Wahab et al., 2014
16	Nawasif/Al Buqum	9-0.2	Weinstein and Garfunkel, 2014; Wahab et al., 2014
17	As Sirat	30-25	Weinstein and Garfunkel, 2014; Wahab et al., 2014
18	Tihama Asir	25-20	Weinstein and Garfunkel, 2014; Wahab et al., 2014
19	Yemen/Ataq	30-26; 22-18; 3.5-0	Weinstein and Garfunkel, 2014; Wahab et al., 2014; Rooney, 2017
20	Afar	27-19; 16-9; 8-6; 2.3-1; present	Zumbo et al., 1995; George et al., 1998, Chernet et al., 1998; Lahitte et al., 2003
21	Northern Ethiopia	33.9-27; 13-9; 3.2-0	Hoffman et al., 1997; George et al., 1998; Kieffer et al., 2004; Nelson et al., 2012 ; Rooney, 2017
22	S. Ethiopia	45-35; 19-12; 3.5-0	Ebinger et al., 1993; George et al., 1998; Ulkstin et al., 2002; Rooney, 2007, 2017
23	Northern Kenya (Turkana)	40-30; 26-16; 3.5-0	Furman et al., 2004, 2006; Meshesha and Shinjo, 2008 Nelson et al., 2012; Rooney, 2017
24	Central Kenya	15-9; 6-3; 3-1.7; 0.7-0	Baker, 1986
25	Northern Tanzania	5.9-2.9; 2.6-1.8; 1.65-0.75; 0.5-0	Mana et al., 2015

Name, magmatic phase time range, and related references for each volcanic site in the East-Africa-Arabia region. We refer to Figure 2B for the location of the volcanic sites and to Supplementary Text S1 for more details about the eruption age compilation.

Supplementary Table S2

Network code	Station name	Longitude (deg)	Latitude (deg)	Data center (and seismic experiment)
1B	kabe	30.47	0.87	GEOFON, http://geofon.gfz-potsdam.de
1B	kmtw	30.38	0.74	
1B	mwey	29.9	-0.19	
AB	qzx	45.37	41.05	ORFEUS, http://www.orfeus-eu.org
AF	nbi	36.8	-1.27	IRIS, http://www.iris.edu/hq/; AfricaArray, (Nyblade et al., 2008, 2011)
G	atd	42.85	11.53	GEOFON, http://geofon.gfz-potsdam.de
GE	ape	25.53	37.07	GEOFON, http://geofon.gfz-potsdam.de
GE	arpr	38.34	39.09	
GE	bgio	35.09	31.72	
GE	css	33.33	34.96	
GE	damy	44.39	14.57	
GE	eil	34.95	29.67	
GE	ghaj	35.57	31.3	
GE	isp	30.51	37.84	
GE	jer	35.2	31.77	
GE	karp	27.16	35.55	
GE	kibk	38.04	-2.36	
GE	kmbo	37.25	-1.13	
GE	kris	25.5	35.18	
GE	ksdi	35.66	33.19	
GE	last	25.48	35.16	
GE	lodk	35.36	3.42	
GE	malt	38.43	38.31	
GE	mrni	35.39	33.12	
GE	msbi	35.36	31.31	
GE	nai	36.8	-1.27	

GE	sant	25.46	36.37	
GE	socy	53.99	12.52	
GE	ujap	35.46	31.95	
GE	zkr	26.22	35.11	
GO	akh	43.49	41.41	IRIS, http://www.iris.edu/hq/; National Seismic Network of Georgia (Tumanova et al., 2016)
GO	ddfl	46.12	41.45	
GO	lgd	46.24	41.83	
GO	oni	43.45	42.59	
GO	tblg	44.74	41.73	
HL	ape	25.53	37.07	NOA, http://bbnet.gein.noa.gr; HUSN (D'Alessandro et al., 2011; Evangelidis & Melis, 2012)
HL	karp	27.16	35.55	
HL	rdo	25.54	41.15	
HL	sant	25.46	36.37	
HT	aln	26.05	40.9	NOA, http://bbnet.gein.noa.gr; AUTHnet (Pitilakis et al., 2016)
HT	chos	26.05	38.39	
HT	sigr	25.86	39.21	
II	mbar	30.74	-0.6	IRIS, http://www.iris.edu/hq/
II	msey	55.48	-4.67	
II	rayn	45.5	23.52	
II	uoss	56.2	24.95	
IS	amaz	34.92	31.53	GEOFON, http://geofon.gfz-potsdam.de

IS	eil	34.95	29.67	
IS	hrfi	35.03	30.04	
IS	jer	35.2	31.77	
IS	ksdi	35.66	33.19	
IS	kzit	34.4	30.91	
IS	mmli	35.42	32.44	
IU	anto	32.79	39.87	IRIS, http://www.iris.edu/hq/)
IU	furi	38.68	8.9	
IU	gni	44.74	40.15	
IU	kmbo	37.25	-1.13	
IU	nai	36.8	-1.27	
JS	aqbj	35.05	29.73	GEOFON, http://geofon.gfz-potsdam.de; Jordan Seismic Network (Rodgers et al., 2003)
KO	agrb	42.99	39.58	KOERI, http://www.koeri.boun.edu.tr/new/
KO	alt	30.11	39.06	
KO	balb	27.88	39.64	
KO	bnn	35.85	38.85	
KO	bzk	34	41.96	
KO	edrb	26.74	41.85	
KO	ell	29.91	36.75	
KO	gada	25.9	40.19	
KO	gaz	37.21	37.17	
KO	guro	42.03	38.55	
KO	ikl	33.69	36.24	
KO	isk	29.06	41.07	
KO	kars	43.09	40.62	
KO	kula	28.66	38.51	
KO	mdub	31.2	40.47	
KO	ptk	39.39	38.89	
KO	rsdy	37.33	40.4	
KO	sirt	42.44	37.5	
KO	snop	35.21	42.02	
KO	vanb	43.39	38.6	

KW	mib	47.34	29.8	IRIS, http://www.iris.edu/hq/
MN	keg	31.83	29.93	INGV, https://www.ingv.it
ZD	kris	25.5	35.18	GEOFON, http://geofon.gfz-potsdam.de
TU	andn	36.35	37.58	KOERI, http://www.koeri.boun.edu.tr/new/; TNSN (Al-Lazki et al., 2003)
TU	aydn	27.88	37.66	
TU	bora	30.45	39.88	
TU	digo	43.37	40.41	
TU	erba	36.75	40.68	
TU	hakt	43.71	37.56	
TU	ilga	33.72	41.05	
TU	kelt	39.26	40.15	
TU	kema	38.49	39.27	
XD	baso	35.14	-4.32	IRIS, http://www.iris.edu/hq/; TBSN (Brazier et al., 2000; Nyblade et al., 1996)
XD	goma	29.69	-4.84	
XD	komo	36.72	-3.84	
XD	kond	35.8	-4.9	
XD	long	36.7	-2.73	
XD	mbwe	34.35	-4.96	
XD	puge	33.18	-4.71	
XD	sing	34.73	-4.64	
XD	tara	36.02	-3.89	
XG	agin	38.71	38.94	IRIS, http://www.iris.edu/hq/; Eastern Turkey Seismic Experiment (Sandvol et al., 2003)

XG	ahlt	42.48	38.75	
XG	bngl	40.6	38.92	
XG	btls	42.12	38.43	
XG	bYBt	40.27	40.24	
XG	bykn	41.78	38.17	
XG	cmcy	43.2	39.92	
XG	dgrl	43.33	41.06	
XG	dgsu	42.73	39.13	
XG	dYBr	40.32	37.82	
XG	ergn	39.73	38.26	
XG	eZRm	41.36	40.1	
XG	hamr	42.99	39.61	
XG	hins	41.7	39.35	
XG	hrpt	39.25	38.7	
XG	hrsn	42.29	39.95	
XG	ilic	38.57	39.45	
XG	imrl	38.12	39.88	
XG	kars	43.07	40.62	
XG	kotk	43.01	40.22	
XG	krlv	40.99	39.37	
XG	ktln	41.71	37.95	
XG	kypr	41.17	37.56	
XG	mrdn	40.7	37.29	
XG	msdy	37.78	40.46	
XG	mush	41.48	38.76	
XG	siln	41.04	38.14	
XG	sirn	39.12	40.2	
XG	uzml	39.72	39.71	
XH	ayd	27.84	37.84	IRIS, http://www.iris.edu/hq/
XH	boz	28.05	38.3	
XH	deu	27.21	38.37	
XH	kul	28.63	38.54	
XI	aaus	38.77	9.03	IRIS, http://www.iris.edu/hq/; EKBSE (Bastow et al., 2008; Benoit et al., 2006; Hammond et al., 2013; Nyblade & Langston,

				2002), SABA (Sandvol et al., 1998, 2001)
XI	afif	43.04	23.93	
XI	anga	36.8	-2.5	
XI	arba	37.56	6.07	
XI	bahi	37.39	11.57	
XI	bela	38.47	6.93	
XI	birh	39.53	9.67	
XI	bish	42.69	19.92	
XI	chef	38.21	6.16	
XI	dele	36.33	8.44	
XI	diya	39.6	11.83	
XI	dmrk	37.73	10.31	
XI	fich	38.74	9.78	
XI	goba	39.98	7.03	
XI	gude	37.77	8.97	
XI	halm	44.32	22.85	
XI	hero	39.28	7.03	
XI	hirn	41.11	9.22	
XI	hosa	37.86	7.56	
XI	jima	36.83	7.68	
XI	naza	39.29	8.57	
XI	neke	36.52	9.09	
XI	rani	42.78	21.31	
XI	rayn	45.5	23.52	
XI	riyd	46.64	24.72	
XI	sela	39.13	7.97	
XI	soda	42.38	18.29	
XI	taif	40.35	21.28	
XI	tend	41	11.79	
XI	terc	37.17	7.14	
XI	wane	40.65	10.17	
XI	wash	40.17	8.99	
XJ	ln15	36.18	-2.63	IRIS, http://www.iris.edu/hq/; EAGLE (Bastow et al., 2005; Mackenzie et al., 2005; Maguire et al.,

				2003; Stuart et al., 2002)
XJ	ng54	35.36	-2.73	
XW	w04	28.09	39.92	IRIS, http://www.iris.edu/hq/; YOCMAL (Ahmed et al., 2013; Leroy et al., 2007)
XW	w09	27.9	39	
XY	cam	27.39	37.88	RESIF, https://www.resif.fr; SIMBAAD (Paul et al., 2008)
XY	cdk	32.18	40.97	
XY	evk	27.61	39.02	
XY	gun	29.49	37.51	
XY	kar	30.66	41.04	
XY	kas	29.68	36.21	
XY	koy	27.16	39.54	
XY	lia	25.18	39.9	
XZ	s06	54.05	17.62	IRIS, http://www.iris.edu/hq/; Dhofar (Basuyau et al., 2010)
XZ	s07	54.49	17.25	
XZ	s09	54.7	16.99	
XZ	s10	54.2	17.5	
YB	a1	51.31	29.44	IRIS, http://www.iris.edu/hq/; Kaapvaal Project (Silver et al., 2016)
YB	a2	51.78	29.79	
YB	at31	34.51	38.57	
YB	b2	52.5	30.19	
YB	b3	53.06	30.13	
YB	c2	53.81	32.15	
YF	aper	27.17	35.55	IRIS, http://www.iris.

				edu/hq/; Africa Array (Nyblade et al., 2011)
YF	koum	26.84	37.7	
YJ	adee	39.91	7.79	IRIS, http://www.iris.edu/hq/, EAGLE (Bastow et al., 2005; Mackenzie et al., 2005; Maguire et al., 2003; Stuart et al., 2002)
YJ	adue	38.9	8.54	
YJ	amme	39.09	8.3	
YJ	anke	39.73	9.59	
YJ	aree	39.42	8.94	
YJ	asee	39.13	7.97	
YJ	awae	40.17	8.99	
YJ	bede	40.77	8.91	
YJ	bore	39.55	8.75	
YJ	bute	38.38	8.12	
YJ	chae	38.76	9.31	
YJ	dike	39.56	8.06	
YJ	done	39.55	8.51	
YJ	dZEe	39	8.78	
YJ	gewe	40.57	10.01	
YJ	gtfe	39.84	9	
YJ	hire	41.11	9.22	
YJ	inee	39.14	9.9	
YJ	kare	39.93	10.42	
YJ	kote	39.4	9.39	
YJ	leme	38.61	8.61	
YJ	mece	40.32	8.59	
YJ	meke	38.83	8.16	
YJ	mele	40.2	9.31	
YJ	miee	40.76	9.24	
YJ	nure	39.8	8.73	
YJ	sene	39.02	9.15	
YJ	shee	39.89	10	
YJ	wole	37.98	8.53	

YR	ale	42.03	9.42	RESIF, https://www.resif.fr; RLBM (Sebai et al., 2006)
YR	aydo	53.36	16.99	
YR	ayno	53.89	17.26	
YR	bano	54.44	17.69	
YR	daho	54.35	17.53	
YR	dmto	55.07	17.73	
YR	dss	39.64	11.12	
YR	hado	55.19	17.22	
YR	haso	55.22	17.49	
YR	hayo	53.34	17.18	
YR	mado	54.38	17.2	
YR	mdyo	53.36	17.46	
YR	mugo	53.77	16.9	
YR	nnmo	54.25	17.36	
YR	qaly	53.49	12.69	
YR	raho	53.81	17.06	
YR	saho	54.68	17.11	
YR	say	44.2	15.35	
YR	shio	54.17	17.19	
YR	sooo	54.88	17.08	
YR	tqho	54.43	17.06	
YR	yaf	45.25	13.87	
YZ	seme	41.00	11.79	IRIS, http://www.iris.edu/hq/; Afar Urgency Array (Ebinger et al., 2008; Keir et al., 2009)
Z3	amos	25.77	36.8	GEOFON, http://geofon.gfz-potsdam.de; EGELADOS (Friederich & Meier, 2008)
Z3	anaf	25.78	36.36	
Z3	ikar	26.31	37.64	
Z3	kapa	27.14	35.64	
Z3	kaso	26.92	35.41	

Z3	kosi	26.95	36.74	
Z3	lero	26.84	37.16	
Z3	myko	25.38	37.48	
Z3	neak	25.4	36.41	
Z3	rhon	28.08	36.38	
Z3	rhos	27.82	36.01	
Z3	samo	26.84	37.7	
Z3	tilo	27.35	36.45	
Z3	tur1	26.87	38.09	
Z3	tur2	27.24	37.64	
Z3	tur3	27.54	37.47	
Z3	tur4	27.81	37.08	
Z3	tur5	27.32	37.03	
Z3	tur6	28.43	37.02	
Z3	tur7	27.57	36.7	
Z3	tur8	28.94	36.83	
Z3	tur9	28.09	36.7	
Z4	ib09	35.4	31.23	GEOFON, http://geofon.gfz-potsdam.de; DESIRE (Mechie et al., 2009)
Z4	ib15	35.46	31.14	
Z4	ib19	35.44	31.07	
Z4	ib21	35.42	31.02	
Z4	ib22	35.36	31.06	
Z4	ib36	35.39	30.93	
Z4	is02	35.23	31.26	
Z4	is08	35.38	31.24	
Z4	is10	35.41	31.22	
Z4	is16	35.46	31.12	
Z4	is20	35.43	31.05	
Z4	is27	35.28	31.15	
Z4	is32	35.35	31.35	
Z4	is34	35.33	31.07	
Z4	jb01	35.48	31.24	
Z4	jb04	35.43	31.25	
Z4	jb07	35.48	31.29	
Z4	jb10	35.49	31.34	
Z4	jb12	35.5	31.37	
Z4	jb21	35.67	31.2	

Z4	jb37	35.67	31.39	
Z4	jb39	35.61	31.19	
Z4	jb41	35.54	31.27	
ZE	afme	40.86	13.2	IRIS, http://www.iris.edu/hq/; Afar Consortium NSF (Belachew et al., 2011)
ZE	awee	40.07	12.07	
ZE	bare	40.36	12.64	
ZE	bere	41.19	12.17	
ZE	bree	41.19	12.17	
ZE	chie	40.02	11.6	
ZE	dame	40.96	11.69	
ZE	dige	40.27	12.33	
ZE	fine	40.32	12.07	
ZE	hare	40.88	11.61	
ZE	mege	41.34	11.49	
ZE	mile	40.76	11.42	
ZE	rode	40.98	12.84	
ZE	sehe	40.98	12.04	
ZE	seme	41	11.79	
ZE	sile	41.19	12.41	
ZE	true	40.32	12.48	
ZF	abae	39.76	13.35	IRIS, http://www.iris.edu/hq/; Afar Consortium NERC, (Hammond et al., 2011)
ZF	adte	40.76	11.12	
ZF	adye	38.98	13.64	
ZF	akee	39.17	10.89	
ZF	asye	41.44	11.56	
ZF	awse	40.17	8.99	
ZF	bobe	42.57	10.38	
ZF	btie	40.02	11.19	
ZF	dere	39.64	11.12	
ZF	dice	41.57	11.91	
ZF	elle	40.38	11.26	
ZF	erte	40.5	13.45	

ZF	gase	38.92	11.68	
ZF	gewe	40.57	10	
ZF	hale	40.01	13.84	
ZF	hyne	42.1	9.31	
ZF	kobe	39.63	12.15	
ZF	kore	39.93	10.43	
ZF	lale	39.04	12.03	
ZF	lyde	41.93	12.05	
ZF	maye	39.53	12.78	
ZF	mise	40.76	9.24	
ZF	qate	41.47	9.38	
ZF	seke	39.03	12.62	
ZF	smre	39.21	13.2	
ZF	srde	41.31	11.96	
ZF	wlde	39.59	11.82	
ZF	wuce	39.61	11.51	
ZF	yaye	38	11.86	
ZH	y6	49.25	33.98	RESIF, https://www.resif.fr
ZP	bend	31.39	0.58	IRIS, http://www.iris.edu/hq/; Africa Array (Nyblade et al., 2008, 2011)
ZP	biha	31.32	-2.64	
ZP	bkba	31.81	-1.36	
ZP	buti	31.33	1.82	
ZP	fopo	30.28	0.66	
ZP	geit	32.22	-2.88	
ZP	hama	32.64	-3.83	
ZP	jnja	33.18	0.45	
ZP	kate	29.87	-0.14	
ZP	kble	29.99	-1.25	
ZP	kgma	29.63	-4.88	
ZP	kibo	30.71	-3.58	
ZP	male	34.17	1.07	
ZP	maus	36.7	-2.74	
ZP	mkre	30.42	-4.28	
ZP	mlba	31.67	-1.84	
ZP	roti	33.6	1.63	

ZP	saka	31.74	-0.31	
ZP	sulu	30.09	-4.57	
ZR	id07	34.77	30.79	GEOFON, http://geofon.gfz-potsdam.de; DESERT (Mechie et al., 2005; Mohsen et al., 2006)
ZR	id08	34.79	30.6	
ZR	id10	34.49	31.36	
ZR	id12	34.92	30.99	
ZR	id26	34.64	30.97	
ZR	id27	35.24	30.66	
ZR	id28	35.16	30.36	
ZR	id29	35.12	31.36	
ZR	id31	35.13	30.08	
ZR	id32	35.06	29.97	
ZR	id33	35	29.91	
ZR	jd01	35.48	31.24	
ZR	jd02	35.41	30.81	
ZR	jd05	35.23	30.26	
ZR	jd08	35.05	29.72	
ZR	jk02	35.56	30.57	
ZR	js02	36.24	30.29	
ZR	js05	35.81	29.43	
ZR	js07	35.39	29.42	
ZR	jw01	35.97	30.87	
ZU	glum	36.19	-2.62	IRIS, http://www.iris.edu/hq/
ZZ	anaf	25.78	36.36	GEOFON, http://geofon.gfz-potsdam.de; CYCNET/LIBNET (Bohnhoff et al., 2006)
ZZ	asty	26.41	36.58	
ZZ	iosi	25.36	36.74	
ZZ	myko	25.38	37.48	
ZZ	neak	25.4	36.41	

All seismic stations (network code, station code, longitude, latitude and data center) used in the tomographic inversion.

Supplementary Fig. S1.

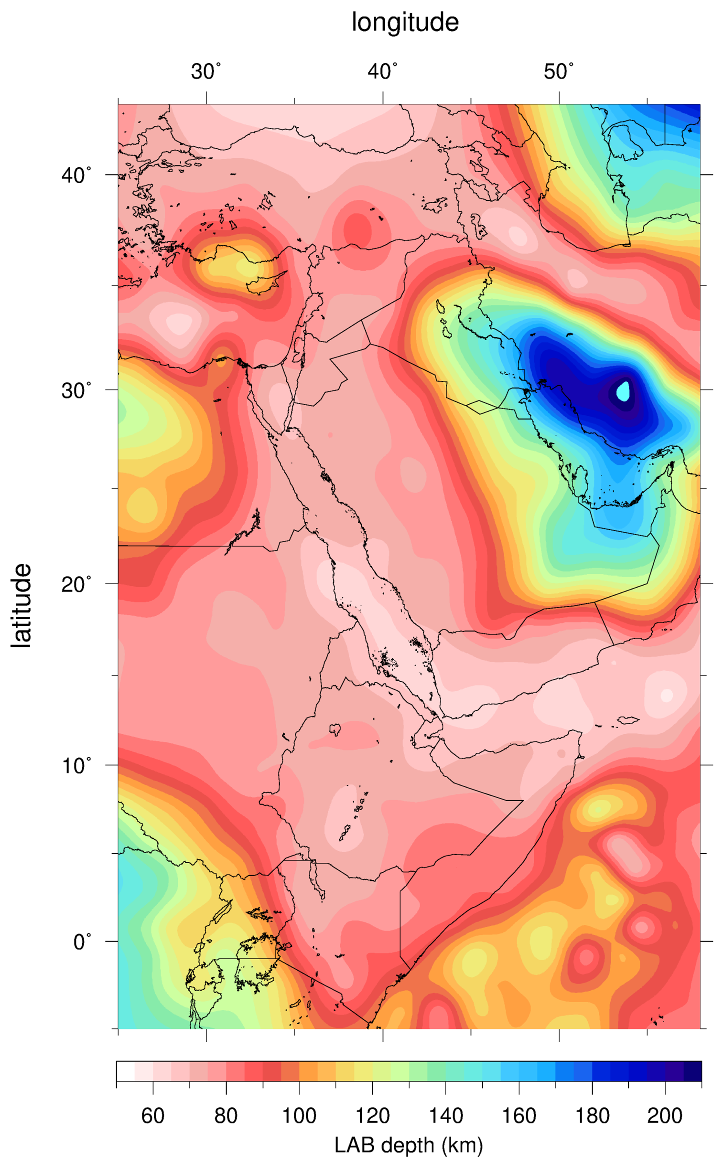

Lithosphere-asthenosphere boundary (LAB) depth map. According to the new WINTERC model of Fullea et al. (2021) The lithosphere is relatively thin (~60-90 km depth) where prominent low-velocity anomalies are imaged, i.e., the three branches of the star-shaped low-velocity centered in Afar. Below the Arabian Platform and Zagros the LAB is deeper, reaching depths greater than 200 km.

Supplementary Fig. S2.

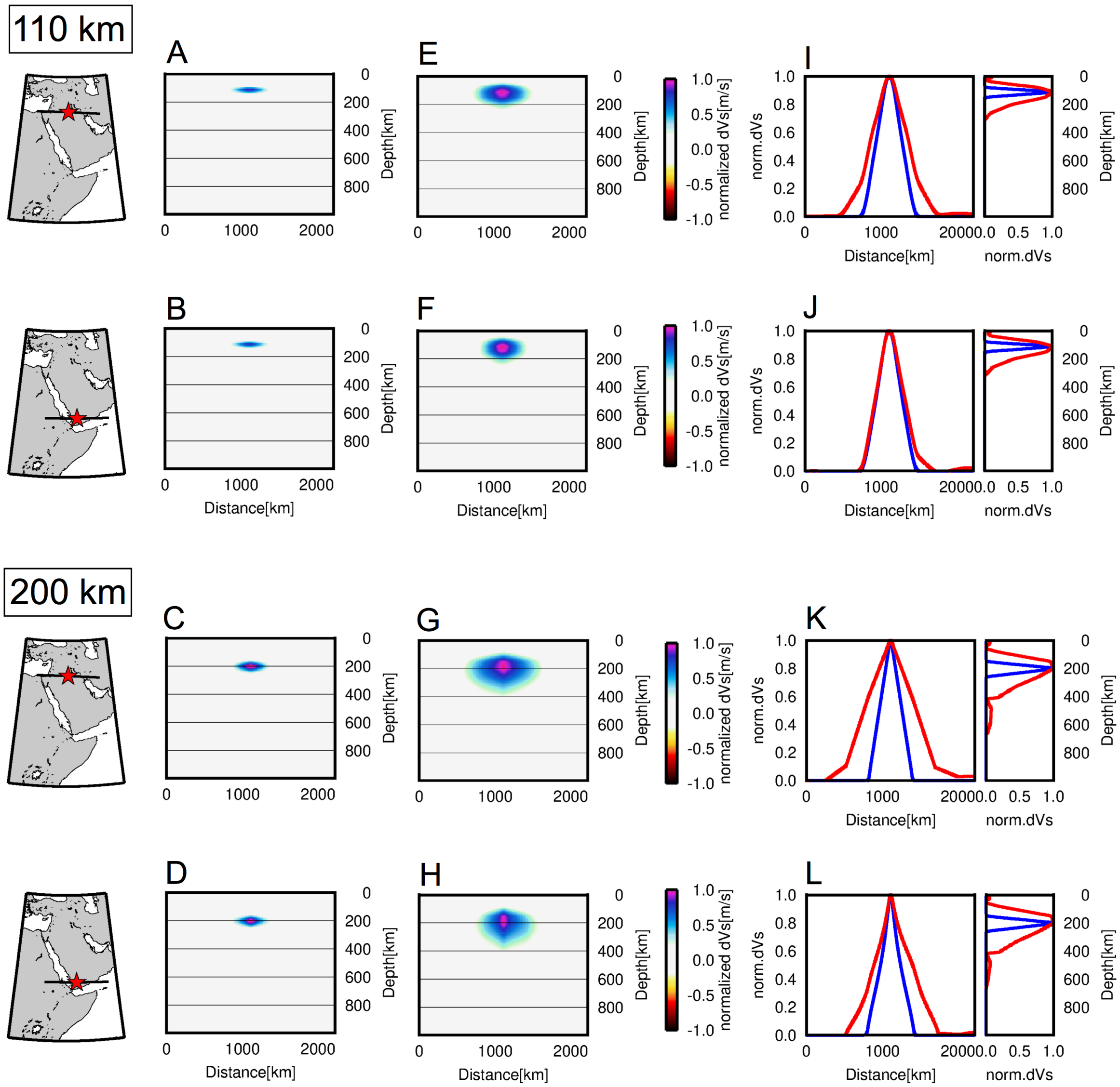

Resolution tests with spike anomalies at 110 and 200 km depth. The locations of the spikes are shown on the maps (left) as red stars. **A-D)** Cross-sections of the two spikes through the input model. **E-H)** Cross-sections through the output model. Orientation of the cross-section is shown on the maps in black. **I-L)** Vertical and horizontal 1D *S*-wave anomaly profiles along the cross-sections. Input profiles are shown in blue, output in red. All *S*-wave velocity anomalies are normalized to the maximum.

Supplementary Fig. S3.

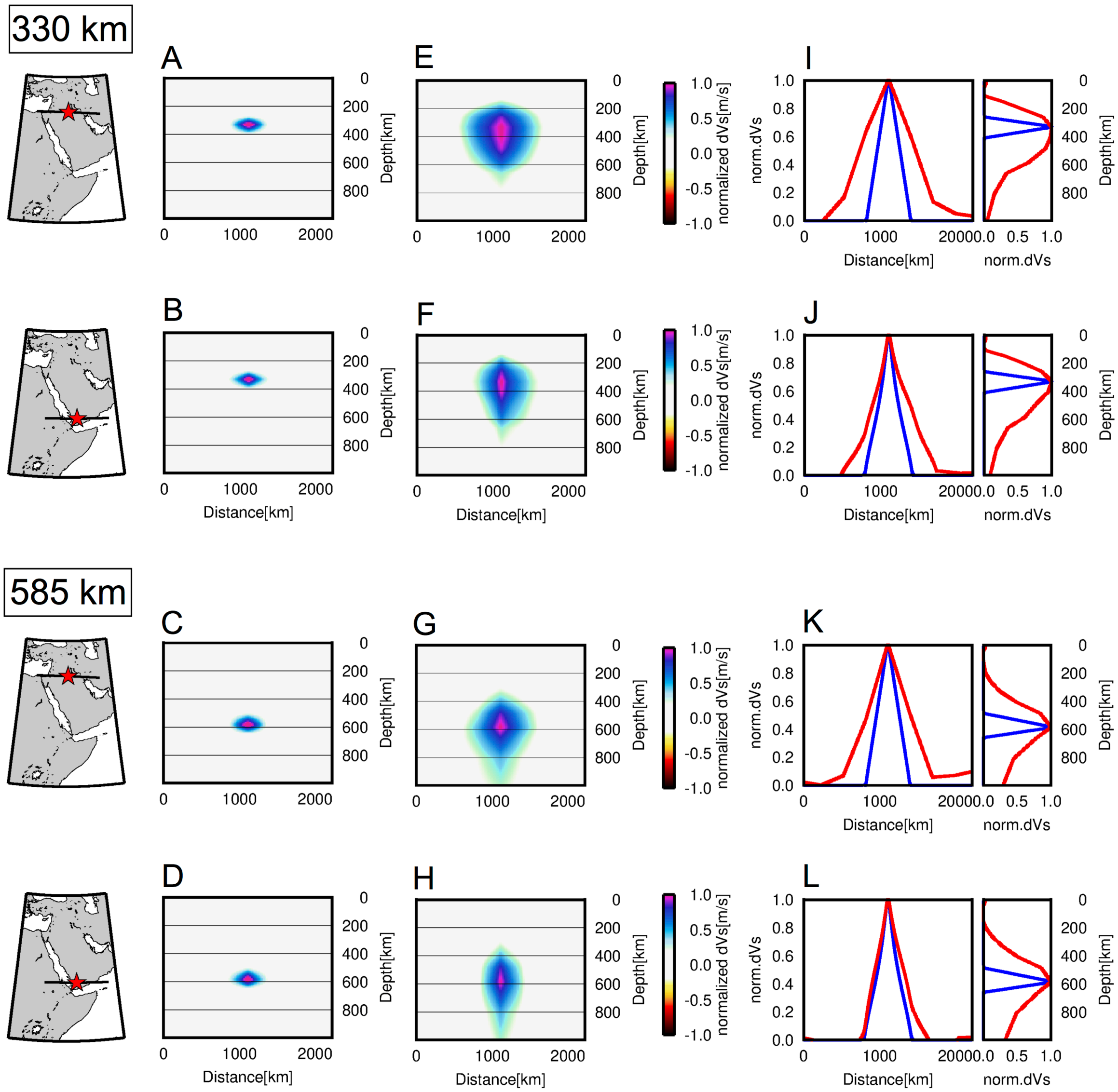

Resolution tests with spike anomalies at 330 and 585 km depth. The locations of the spikes are shown on the maps (left) as red stars. A-D) Cross-sections of the two spikes through the input model. E-H) Cross-sections through the output model. Orientation of the cross-section is shown on the maps in black. I-L) Vertical and horizontal 1D *S*-wave anomaly profiles along the cross-sections. Input profiles are shown in blue, output in red. All *S*-wave velocity anomalies are normalized to the maximum.

Supplementary Fig. S4.

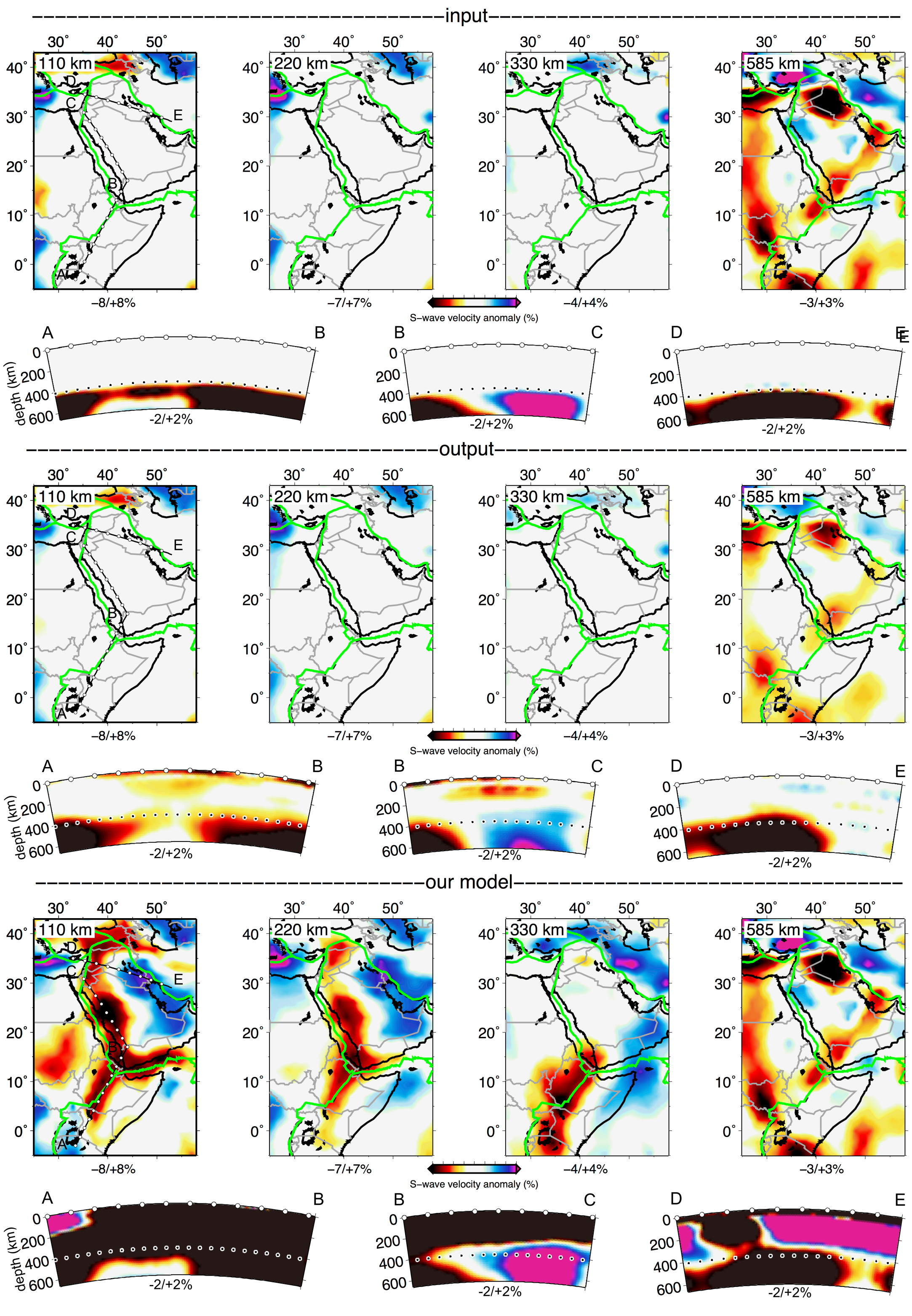

Structural resolution test 2. The velocity anomalies are removed in the input (top panels) at depths shallower than 410 km depth. The output model (middle panels) shows that most of the structure removed does not appear in the upper mantle above 410 km depth. The magnitude of the spurious structure below East Africa-Arabia is weaker than that imaged in our model (bottom panels). The orientations of the cross-sections are plotted in the 110-km depth slice and are the same as those in Figure 4. Major plate boundaries are plotted as green lines. White points indicate the distance every 2°. The dotted line in the cross-sections indicates the 410-km depth discontinuity.

Supplementary Fig. S5.

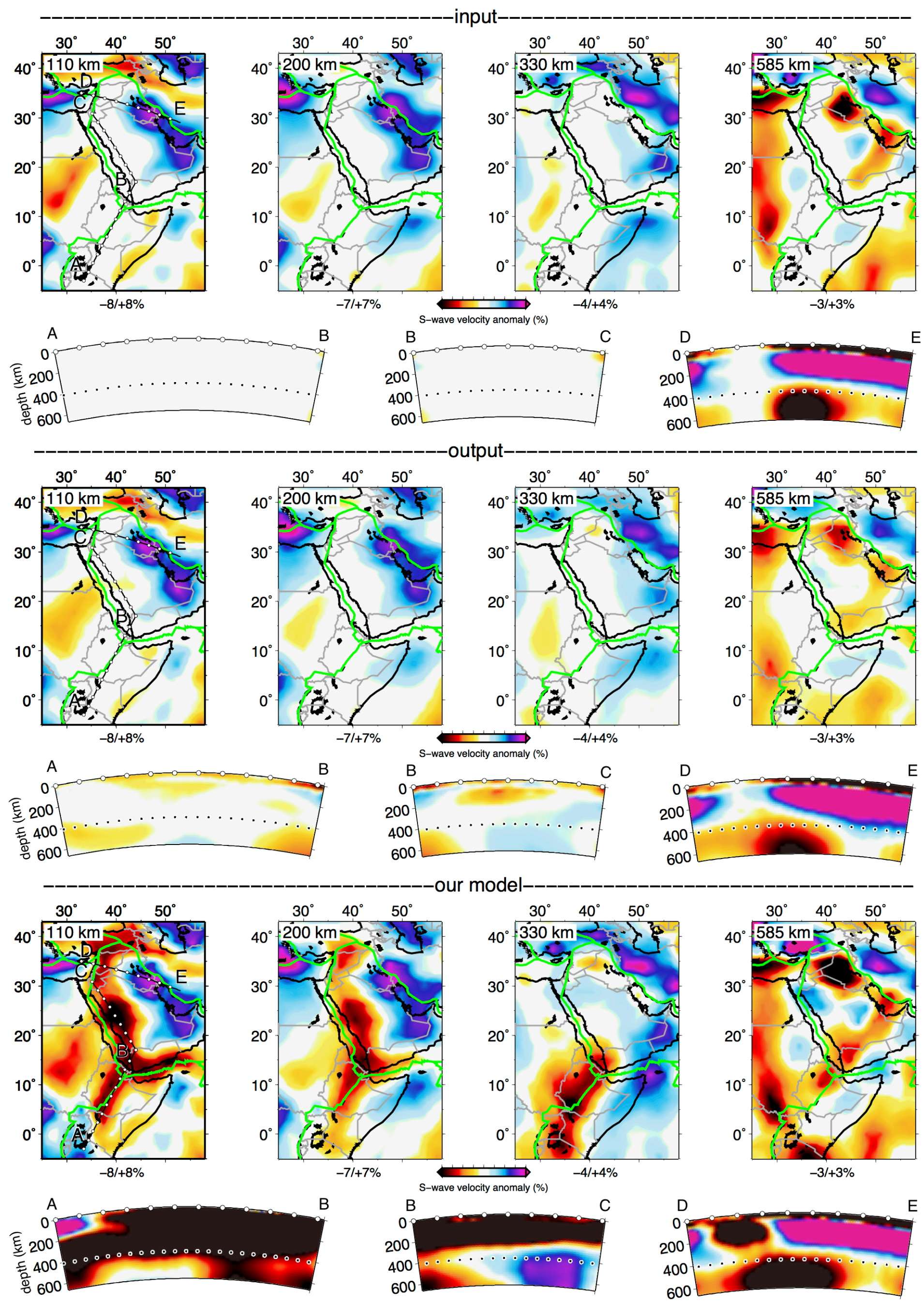

Structural resolution test 3. The velocity anomalies below East Africa and the Arabian Shield are removed in the input (top panels) from the surface down to 660 km depth. Only a very weak spurious feature appears below West Arabia at 110 km depth in the output model, confirming that both the upper-mantle curtain-like anomaly below the East African Rift and the low-velocity channel below the Arabian Shield are not artifacts and are required by the data. The orientations of the cross-sections are plotted in the 110-km depth slices and are the same of those of Figure 4. Major plate boundaries are plotted as green lines. White points indicate the distance every 2°. The dotted line in the cross-sections indicates the 410-km depth discontinuity.

Supplementary Fig. S6.

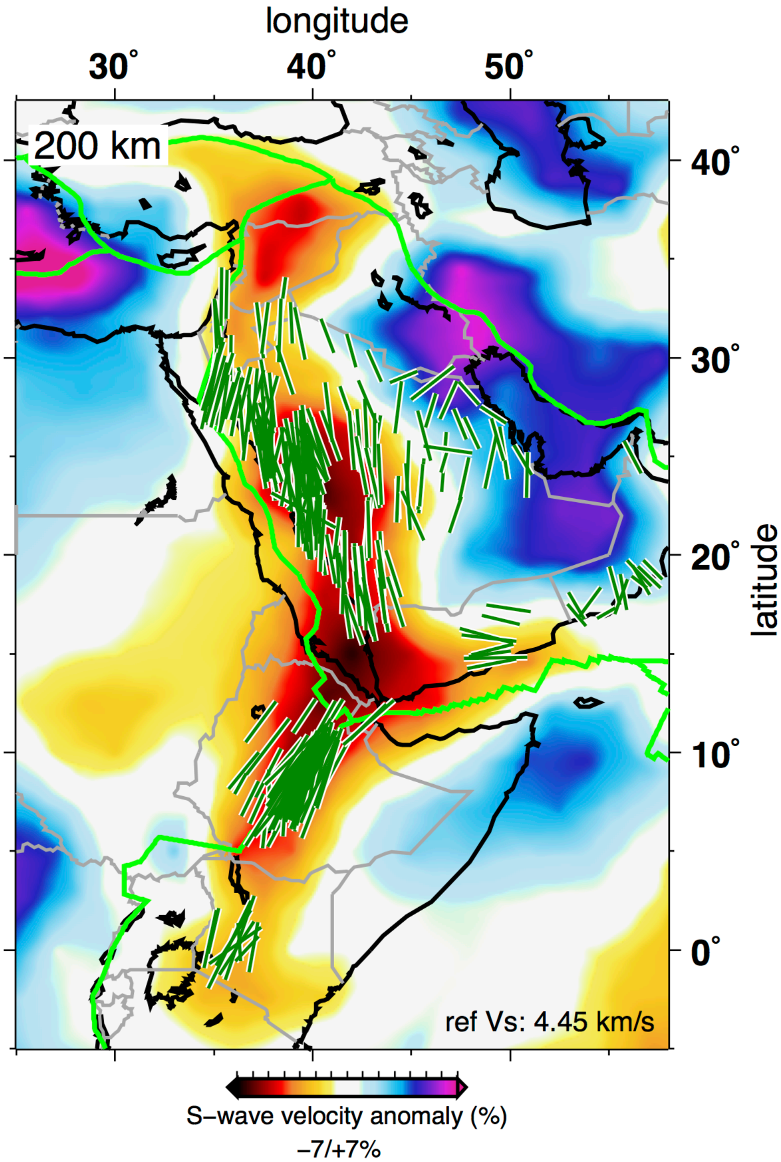

The complete compilation of shear-wave splitting measurements (green bars) for East Africa and Arabia region. The shear-wave splitting measurements are compiled from previous anisotropy studies (from the compilation of Gao et al. 2010; Qaysi et al. 2018). The fast-propagation directions indicate branch-parallel flow of hot plume material within the three branches of the star-shaped low-velocity anomaly. Note, for example, that the orientation of the fast polarization directions is east-west in Yemen, parallel to the strike of the Gulf of Aden branch and to the inferred direction of the hot mantle flow, but different—mostly north-south—in Oman, where the underlying thick lithosphere, indicated by a high-velocity anomaly, impedes the asthenospheric flow.

Supplementary Fig. S7.

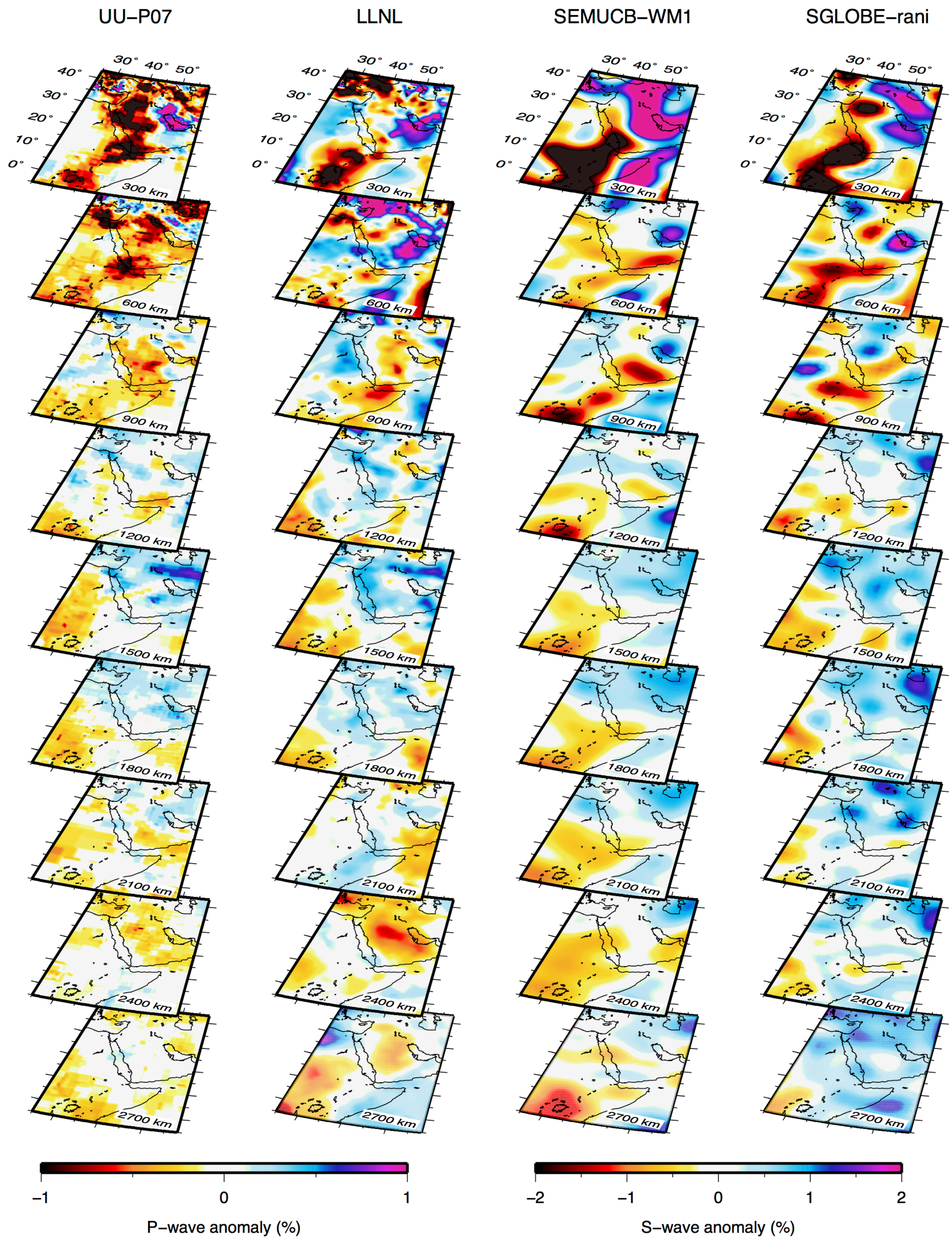

Global tomographic models through the whole mantle. Tomographic depth slices are shown for the following whole-mantle tomography models: the P-wave model UU-P07 (Amaru, 2007) in the first column; the P-wave model LLNL (Simmons et al., 2012) in the second column; the S-wave model SEMUCB-WM1 (French & Romanowicz, 2014) in the third column; and the S-wave model SGLOBE-rani (Chang et al., 2015) in the fourth column.

Supplementary Fig. S8.

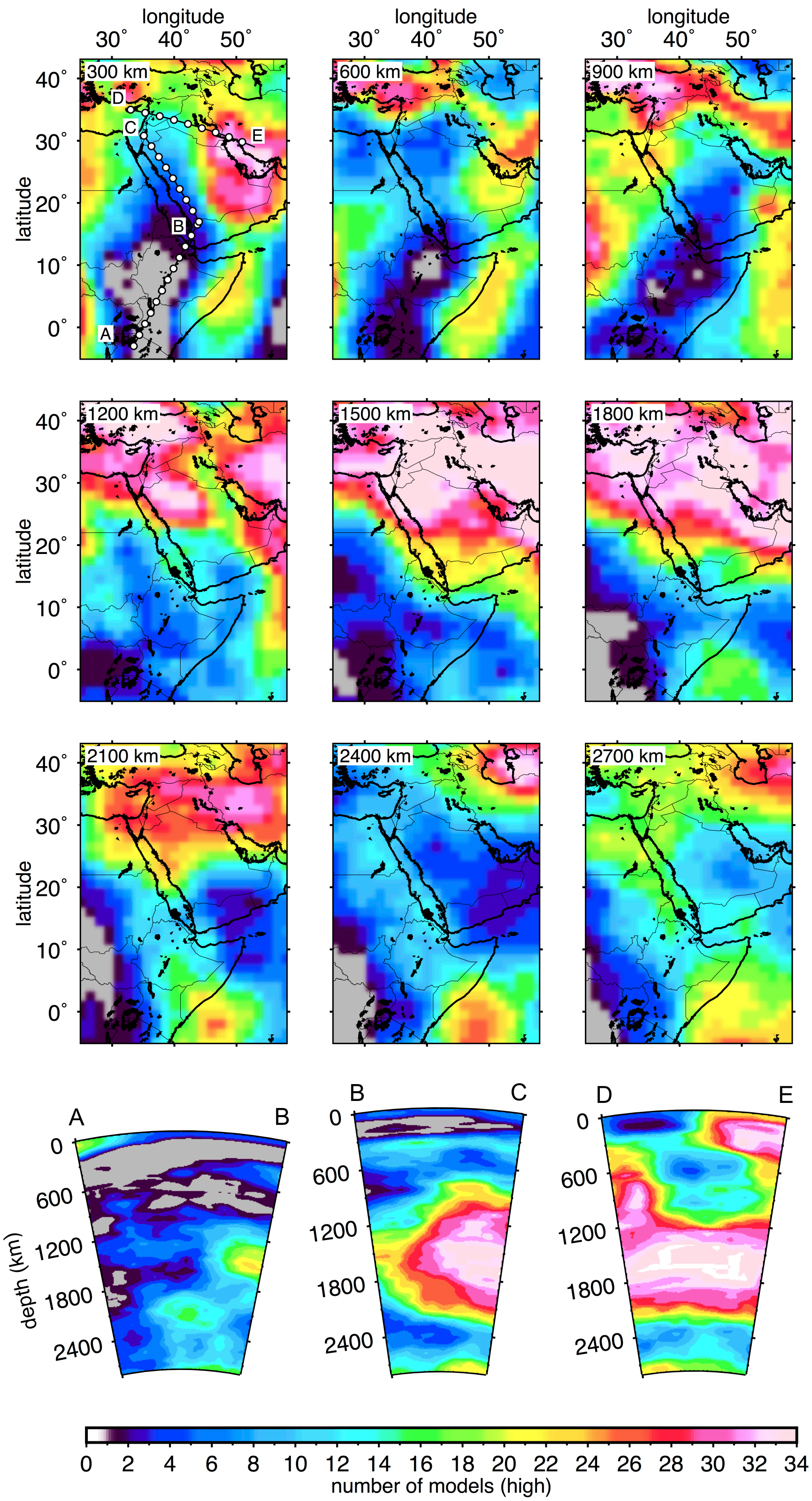

High-velocity vote images of the whole mantle for 34 tomographic models (dv/v > 0). The vote maps and cross-sections are obtained by the joint analysis of the 34 *P*- and *S*-wave models available in the *SubMachine* tomography repository (Hosseini et al., 2018) and serve as a guide in identifying common features from tomographic models. The number of votes at a given location corresponds to the number of models in which a seismically fast velocity anomaly at a given depth is present. The depth slices are shown at 300, 600, 900, 1200, 1500, 1800, 2100, 2400 and 2700 km. The vote maps show a broad high-velocity anomaly below Northern Saudi Arabia and Middle East at ~1200-2100 km depth, probably indicating the Arabian-Mesopotamia slabs subducted during the Late Cretaceous. The orientations of the cross-sections are plotted in the depth slices at 300 km and are the same as those presented in Figure 4. In cross-section AB the majority of models agree that no high-velocity anomalies are present below East Africa. Cross-sections BC and DE indicate a broad positive wavespeed feature between ~1000 and 2000 km depth below West Arabia and Levant region, suggesting the presence of the Arabian subducted slab sinking in the lower mantle.

Supplementary Fig. S9.

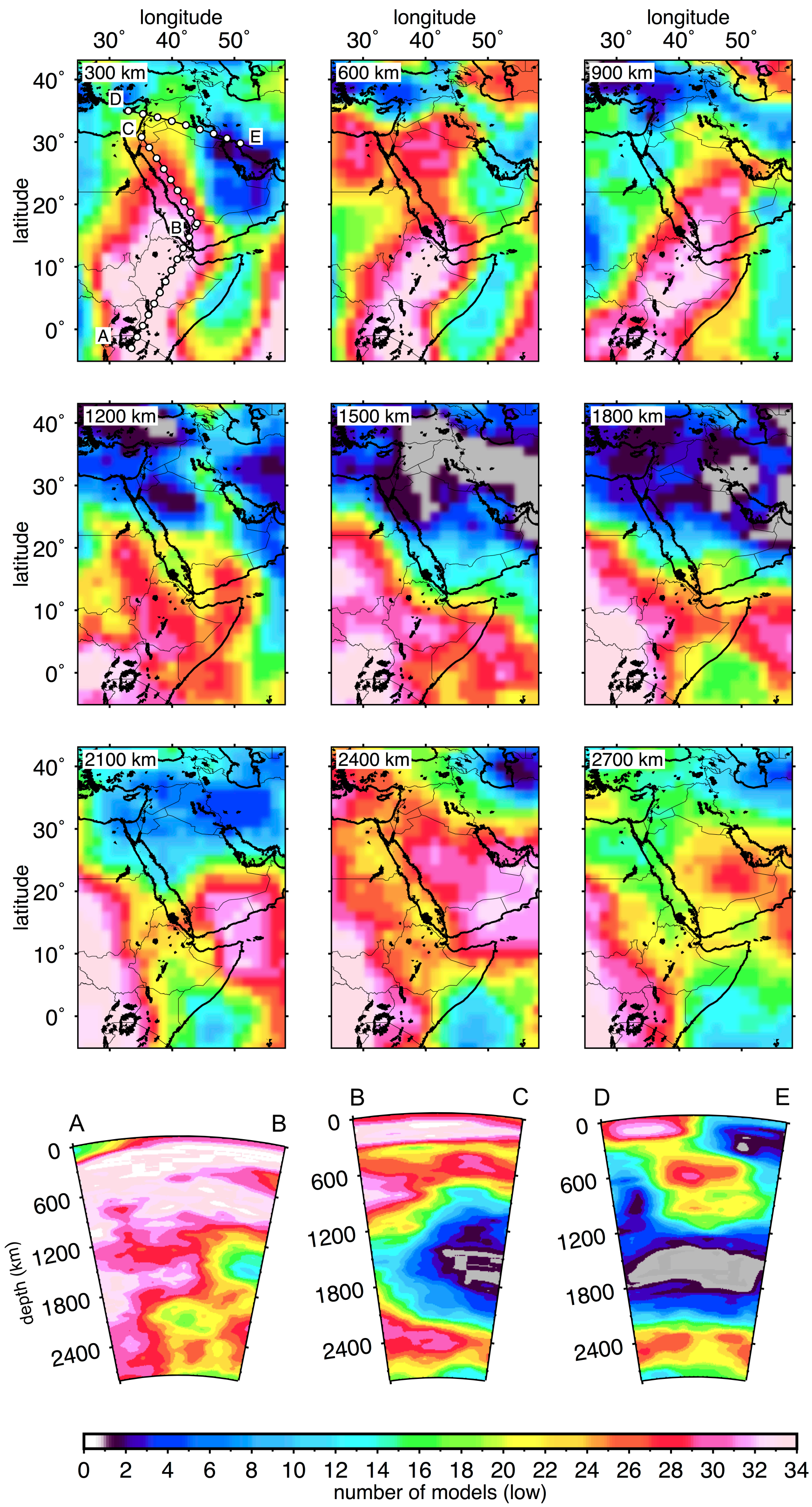

Low-velocity vote images of the whole mantle for 34 tomographic models (dv/v < 0). The vote maps and cross-sections are obtained by the joint analysis of *P*- and *S*-wave models available in the *SubMachine* tomography repository (Hosseini et al., 2018). The number of votes at a given location corresponds to the number of models in which a seismically slow velocity anomaly at a given depth is present. The models are those used in Supplementary Figure S8. The vote maps highlight a broad low-velocity anomaly below southern Arabia and offshore Somalia at 2100-2400 km depth, which may indicate the deep mantle roots of the LP and AP. Another low-velocity body below Central-East Africa underlies the KP and is likely to be its deep part. The orientations of the cross-sections are plotted in the depth slices at 300 km are the same as those in Figure 4. Cross-section AB shows an overwhelming model agreement on the presence of a low-velocity anomaly below East Africa down to the base of the lower mantle. The maximum vote region is below Kenya and Tanzania. In cross-section BC high vote counts are observed mostly in the asthenosphere beneath West Arabia, in agreement with the low-velocity channel imaged in our model. Cross-section DE captures the shape and extension of the low-velocity anomaly imaged below the Levant region, interpreted as the LP.

Supplementary Fig. S10.

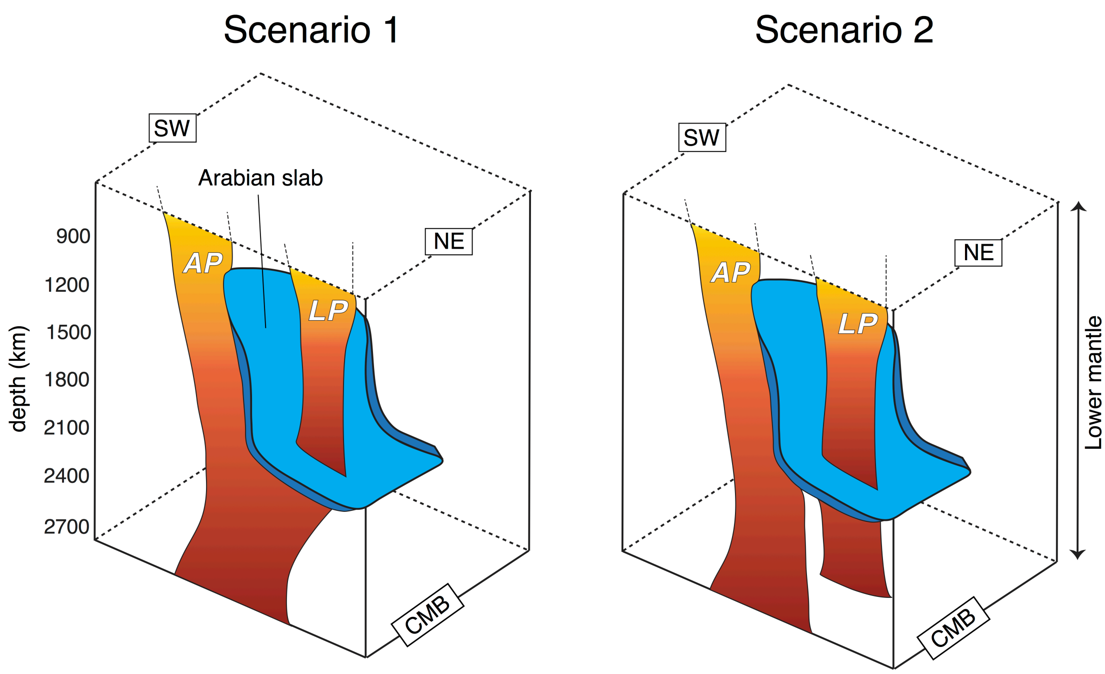

Two proposed scenarios for the source(s) of the Afar and Levant Plumes. Scenario 1 (left panel): the Afar Plume (AP) and Levant Plume (LP) originate at the core-mantle boundary (CMB) from a single source located beneath Arabia and offshore. LP and AP can be splitted in two at mid-mantle depths by the subducted Arabian slab. Scenario 2 (right panel): AP and LP may be originated from two distinct sources in the lowermost mantle and both perturbed by the Arabian slab.

Supplementary Fig. S11.

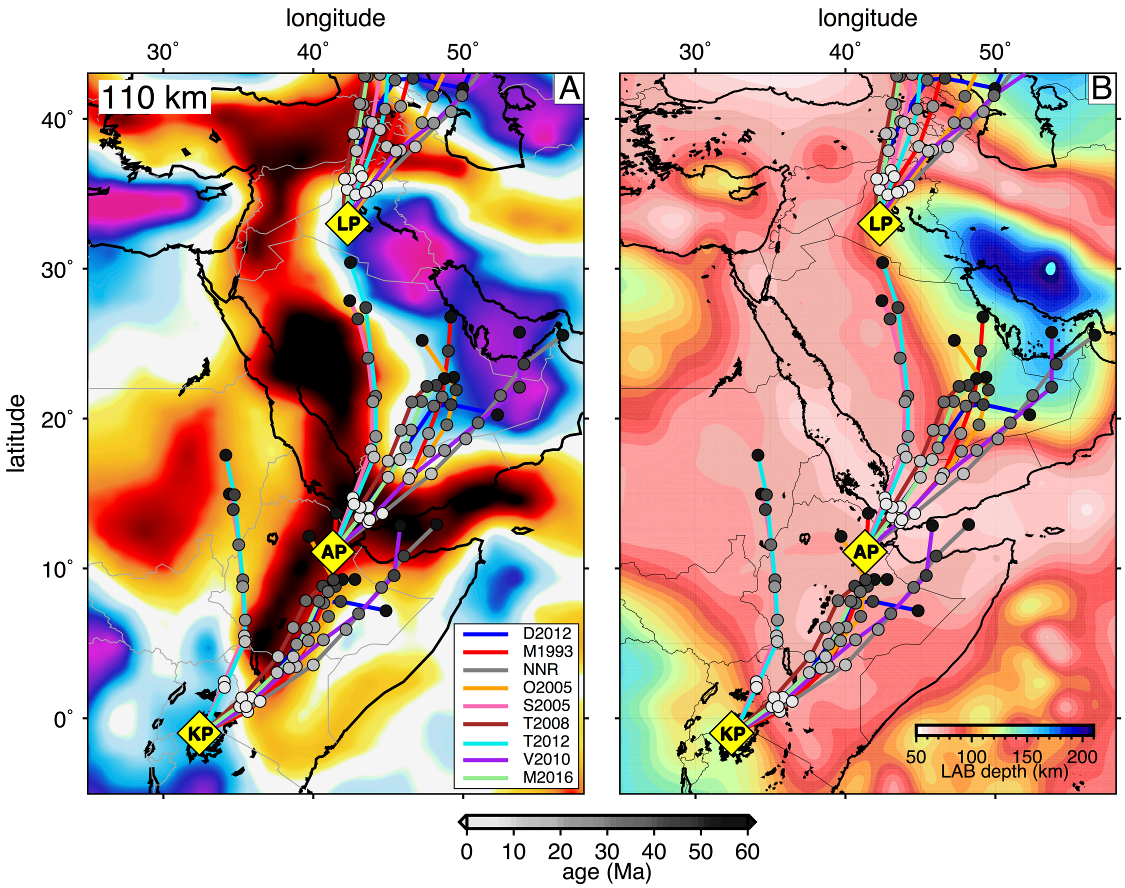

Plume tracks at 0-60 Ma according to different plate-motion models. The models are: D2012 (Doubrovine et al., 2012); M1993 (Muller et al., 1993); NNR (No-Net-Rotation, (Argus et al., 2011); O2005 (O'Neill et al., 2005); S2005 (Schettino & Scotese, 2005); T2008 (Torsvik et al., 2008); T2012 (Torsvik et al., 2012); V2010 (Van Der Meer et al., 2010); M2016 (Matthews et al., 2016). **A.** The map view is the tomographic model plotted at 110 km depth. **B.** The map view is the lithosphere-asthensphere boundary (LAB) depth computed by Fullea et al. (2021). The yellow diamonds indicate the three plumes: KP (Kenya Plume), AP (Afar Plume), and LP (Levant Plume).The different tracks show the variability of results depending on how the plate motion model was built. The dots are coloured according to the age, in Ma.

References

Ahmed, A., Tiberi, C., Leroy, S., Stuart, G. W., Keir, D., Sholan, J., et al. (2013). Crustal structure of the rifted volcanic margins and uplifted plateau ofwestern yemen from receiver function analysis. *Geophysical Journal International*, *193*(3), 1673–1690. https://doi.org/10.1093/gji/ggt072

Al-Lazki, A. I., Seber, D., Sandvol, E., Turkelli, N., Mohamad, R., & Barazangi, M. (2003). Tomographic Pn velocity and anisotropy structure beneath the Anatolian plateau (eastern Turkey) and the surrounding regions. *Geophysical Research Letters*, *30*(24), 4–7. https://doi.org/10.1029/2003GL017391

Aldanmaz, E., Pearce, J. A., Thirlwall, M. F., & Mitchell, J. G. (2000). Petrogenetic evolution of late Cenozoic, post-collision volcanism in western Anatolia, Turkey. *Journal of Volcanology and Geothermal Research*, *102*(1–2), 67–95. https://doi.org/10.1016/S0377-0273(00)00182-7

Amaru, M. L. (2007). Global travel time tomography with 3-D reference models. *Geologica Ultraiectina*, *274*, 174.

Argus, D. F., Gordon, R. G., & Demets, C. (2011). Geologically current motion of 56 plates relative to the no-net-rotation reference frame. *Geochemistry, Geophysics, Geosystems*, *12*(11), 1–13. https://doi.org/10.1029/2011GC003751

Baker, B. H. (1986). Tectonics and volcanism of the southern Kenya Rift Valley and its influence on rift sedimentation. *Geological Society Special Publication*, *25*(25), 45–57. https://doi.org/10.1144/GSL.SP.1986.025.01.05

Baldridge, W. S., Eyal, Y., Bartov, Y., Steinitz, G., & Eyal, M. (1991). Miocene magmatism of sinai related to the opening of the red sea. *Tectonophysics*, *197*(2–4), 181–201. https://doi.org/10.1016/0040-1951(91)90040-Y

Bartol, J., & Govers, R. (2014). A single cause for uplift of the Central and Eastern Anatolian plateau? *Tectonophysics*, *637*, 116–136. https://doi.org/10.1016/j.tecto.2014.10.002

Bastow, I. D., Nyblade, A. A., Stuart, G. W., Rooney, T. O., & Benoit, M. H. (2008). Upper mantle seismic structure beneath the Ethiopian hot spot: Rifting at the edge of the African low-velocity anomaly. *Geochemistry, Geophysics, Geosystems*, *9*(12), Q12022.

Bastow, I. D., Stuart, G. W., Kendall, J. M., & Ebinger, C. J. (2005). Upper-mantle seismic structure in a region of incipient continental breakup: Northern Ethiopian rift. *Geophysical Journal International*, *162*(2), 479–493. https://doi.org/10.1111/j.1365-246X.2005.02666.x

Basuyau, C., Tiberi, C., Leroy, S., Stuart, G., Al-Lazki, A., Al-Toubi, K., & Ebinger, C. (2010). Evidence of partial melting beneath a continental margin: Case of Dhofar, in the Northeast Gulf of Aden (Sultanate of Oman). *Geophysical Journal International*, *180*(2), 520–534. https://doi.org/10.1111/j.1365-246X.2009.04438.x

Belachew, M., Ebinger, C., Coté, D., Keir, D., Rowland, J. V, Hammond, J. O. S., & Ayele, A. (2011). Comparison of dike intrusions in an incipient seafloor - spreading segment in Afar , Ethiopia : Seismicity perspectives, *116*, 1–23. https://doi.org/10.1029/2010JB007908

Benoit, M. H., Nyblade, A. A., Owens, T. J., & Stuart, G. (2006). Mantle transition zone structure and upper mantle S velocity variations beneath Ethiopia: Evidence for a broad, deep-seated thermal anomaly. *Geochemistry, Geophysics, Geosystems*, *7*(11). https://doi.org/10.1029/2006GC001398

Bohnhoff, M., Rische, M., Meier, T., Becker, D., Stavrakakis, G., & Harjes, H. P. (2006). Microseismic activity in the Hellenic Volcanic Arc, Greece, with emphasis on the seismotectonic setting of the Santorini-Amorgos zone. *Tectonophysics*, *423*(1–4), 17–33. https://doi.org/10.1016/j.tecto.2006.03.024

Brazier, R. A., Nyblade, A. A., Langston, C. A., & Owens, T. J. (2000). Pn wave velocities beneath the Tanzania Craton and adjacent rifted mobile belts, East Africa. *Geophysical Research Letters*, *27*(16), 2365–2368. https://doi.org/10.1029/2000GL011586

Camp, V. E., & Roobol, M. J. (1992). Upwelling asthenosphere beneath western Arabia and its regional implications. *Journal of Geophysical Research*, *97*(B11), 15255–15271.

Camp, V. E., Roobol, M. J., & Hooper, P. R. (1991). The Arabian continental alkali basalt province: Part II. Evolution of Harrats Khaybar, Ithnayn, and Kura, Kingdom of Saudi Arabia. *Geological Society of America Bulletin*, *103*, 363–391. https://doi.org/10.1130/0016-7606(1992)104<0379:TACABP>2.3.CO;2

Camp, V. E., Roobol, M. J., & Hooper, P. R. (1989). The Arabian continental alkali basalt province: part III. Evolution of Harrat Kishb, Kingdom of Saudi Arabia. *Geological Society of America Bulletin*, *104*(4), 379–396. https://doi.org/10.1130/0016-7606(1992)104<0379:TACABP>2.3.CO;2

Camp, V. E., Hooper, P. R., Roobol, M. J., & White, D. L. (1987). The Madinah eruption, Saudi Arabia: Magma mixing and simultaneous extrusion of three basaltic chemical types. *Bulletin of Volcanology*, 680–693.

Chang, S. J., Ferreira, A. M. G., Ritsema, J., Heijst, H. J., & Woodhouse, J. H. (2015). Joint inversion for global isotropic and radially anisotropic mantle structure including crustal thickness perturbations, *120*, 4278–4300. https://doi.org/10.1002/2014JB011824.Received

D'Alessandro, A., Papanastassiou, D., & Baskoutas, I. (2011). Hellenic Unified Seismological Network: An evaluation of its performance through SNES method. *Geophysical Journal*

International, *185*(3), 1417–1430. https://doi.org/10.1111/j.1365-246X.2011.05018.x

Deniel, C., Vidal, P., Coulon, C., Vellutini, P. J., & Piguet, P. (1994). Temporal evolution of mantle sources during continental rifting: the volcanism of Djibouti (Afar). *Journal of Geophysical Research*, *99*(B2), 2853–2869. https://doi.org/10.1029/93JB02576

Dilek, Y., & Whitney, D. L. (2000). Cenozoic crustal evolution in Central Anatolia: extension, magmatism and landscape development. In *Proceedings of the Third International Conference on the Geology of the Eastern Mediterranean* (pp. 183–192).

Doubrovine, P. V., Steinberger, B., & Torsvik, T. H. (2016). A failure to reject: Testing the correlation between large igneous provinces and deep mantle structures with EDF statistics. *Geochemistry Geophysics Geosystems*, *17*, 1130–1163. https://doi.org/10.1002/2015GC006205

Doubrovine, P. V., Steinberger, B., & Torsvik, T. H. (2012). Absolute plate motions in a reference frame defined by moving hot spots in the Pacific, Atlantic, and Indian oceans. *Journal of Geophysical Research: Solid Earth*, *117*(9), 1–30. https://doi.org/10.1029/2011JB009072

Ebinger, C. J., Keir, D., Ayele, A., Calais, E., Wright, T. J., Belachew, M., et al. (2008). Capturing magma intrusion and faulting processes during continental rupture: Seismicity of the Dabbahu (Afar) rift. *Geophysical Journal International*, *174*(3), 1138–1152. https://doi.org/10.1111/j.1365-246X.2008.03877.x

Ercan, T., Satir, M., Stenitz, G., Dora, A., Sarifakioglu, E., Adis, C., et al. (1995). Features of the Tertiary Volcanism observed at Biga Penisnsula and Gökçeada, Tavsan Islands. *Bull. Min. Res. Exp*, *117*, 55–86.

Ershov, A. V, & Nikishin, A. M. (2004). Recent geodynamics of the Caucasus-Arabia-East

Africa region. *Geotectonics*, *38*(2), 123–136.

Evangelidis, C. P., & Melis, N. S. (2012). Ambient noise levels in greece as recorded at the hellenic unified seismic network. *Bulletin of the Seismological Society of America*, *102*(6), 2507–2517. https://doi.org/10.1785/0120110319

French, S. W., & Romanowicz, B. A. (2014). Whole-mantle radially anisotropic shear velocity structure from spectral-element waveform tomography. *Geophysical Journal International*, *199*(3), 1303–1327. https://doi.org/10.1093/gji/ggu334

Friederich, W., & Meier, T. (2008). Temporary Seismic Broadband Network Acquired Data on Hellenic Subduction Zone. *Eos, Transactions American Geophysical Union*, *89*(40), 378–378. https://doi.org/10.1029/2008eo400002

Fullea, J., Lebedev, S., Martinec, Z., & Celli, N. L. (2021). WINTERC-grav: mapping the upper mantle thermochemical heterogeneity from coupled geophysical-petrological inversion of seismic waveforms, heat flow, surface elevation and gravity satellite data. *Geophysical Journal International*, *226*(1), 146–191.

Furman, T., Bryce, J. G., Karson, J., & Iotti, A. (2004). East African Rift System (EARS) plume structure: Insights from Quaternary mafic lavas of Turkana, Kenya. *Journal of Petrology*, *45*(5), 1069–1088. https://doi.org/10.1093/petrology/egh004

Furman, T., Kaleta, K. M., Bryce, J. G., & Hanan, B. B. (2006). Tertiary mafic lavas of Turkana, Kenya: Constraints on East African plume structure and the occurrence of high-μ volcanism in Africa. *Journal of Petrology*, *47*(6), 1221–1244. https://doi.org/10.1093/petrology/egl009

Gao, S. S., Liu, K. H., & Abdelsalam, M. G. (2010). Seismic anisotropy beneath the Afar Depression and adjacent areas: Implications for mantle flow. *Journal of Geophysical Research: Solid Earth*, *115*(12), 1–15. https://doi.org/10.1029/2009JB007141

George, R., Rogers, N. W., & Kelley, S. P. (1998). Earliest magmatism in Ethiopia: Evidence for two mantle plumes in one flood basalt province. *Geology*, *26*(10), 923–926. https://doi.org/10.1130/0091-7613(1998)026<0923:EMIEEF>2.3.CO;2

Hammond, J. O. S., Kendall, J. M., Stuart, G. W., Ebinger, C. J., Bastow, I. D., Keir, D., et al. (2013). Mantle upwelling and initiation of rift segmentation beneath the Afar Depression. *Geology*, *41*(6), 635–638. https://doi.org/10.1130/G33925.1

Hammond, J. O. S., Kendall, J. M., Stuart, G. W., Keir, D., Ebinger, C., Ayele, A., & Belachew, M. (2011). The nature of the crust beneath the Afar triple junction: Evidence from receiver functions. *Geochemistry, Geophysics, Geosystems*, *12*(12). https://doi.org/10.1029/2011GC003738

Hofmann, C., Courtillot, V., Féraud, G., Rochette, P., Yirgu, G., & Pik, R. (1997). Timing of the Ethiopian floodbasalt event and implications forplume birthand global change. *Nature*, *246*(5429), 170. https://doi.org/10.1038/246170a0

Hosseini, K., Matthews, K. J., Sigloch, K., Shephard, G. E., Domeier, M., & Tsekhmistrenko, M. (2018). SubMachine: Web-Based Tools for Exploring Seismic Tomography and Other Models of Earth's Deep Interior. *Geochemistry, Geophysics, Geosystems*, *19*(5), 1464–1483. https://doi.org/10.1029/2018GC007431

Ilani, S., Harlavan, Y., Tarawneh, K., Rabba, I., Weinberger, R., Ibrahim, K., et al. (2001). New K-Ar ages of basalts from the Harrat Ash Shaam volcanic field in Jordan: Implications for the span and duration of the upper-mantle upwelling beneath the western Arabian plate. *Geology*, *29*(2), 171–174. https://doi.org/10.1130/0091-7613(2001)029<0171:NKAAOB>2.0.CO;2

Innocenti, F., Agostini, S., Di Vincenzo, G., Doglioni, C., Manetti, P., Savaşçin, M. Y., &

Tonarini, S. (2005). Neogene and Quaternary volcanism in Western Anatolia: Magma sources and geodynamic evolution. *Marine Geology*, *221*(1–4), 397–421. https://doi.org/10.1016/j.margeo.2005.03.016

Keir, D., Hamling, I. J., Ayele, A., Calais, E., Ebinger, C., Wright, T. J., et al. (2009). Evidence for focused magmatic accretion at segment centers from lateral dike injections captured beneath the Red Sea rift in Afar. *Geology*, *37*(1), 59–62. https://doi.org/10.1130/G25147A.1

Keskin, M., Pearce, J. A., & Mitchell, J. G. (1998). Volcano-stratigraphy and geochemistry of collision-related volcanism on the Erzurum-Kars Plateau, northeastern Turkey. *Journal of Volcanology and Geothermal Research*, *85*(1–4), 355–404. https://doi.org/10.1016/S0377-0273(98)00063-8

Kieffer, B., Arndt, N., Lapierre, H., Bastien, F., Bosch, D., Pecher, A., et al. (2004). Flood and shield basalts from Ethiopia: Magmas from the African superswell. *Journal of Petrology*, *45*(4), 793–834. https://doi.org/10.1093/petrology/egg112

Krienitz, M. S., Haase, K. M., Mezger, K., Van Den Bogaard, P., Thiemann, V., & Shaikh-Mashail, M. A. (2009). Tectonic events, continental intraplate volcanism, and mantle plume activity in northern Arabia: Constraints from geochemistry and Ar-Ar dating of Syrian lavas. *Geochemistry, Geophysics, Geosystems*, *10*(4), Q04008.

Lahitte, P., Gillot, P. Y., & Courtillot, V. (2003). Silicic central volcanoes as precursors to rift propagation: The Afar case. *Earth and Planetary Science Letters*, *207*(1–4), 103–116. https://doi.org/10.1016/S0012-821X(02)01130-5

Leroy, S., Lucazeau, F., Razin, P., Manatschal, G., & YOCMAL Team. (2007). Young Conjugate Margins Laboratory in the Gulf of Aden : the YOCMAL project. In *AGU Fall Meeting Abstracts* (Vol. 2007, pp. T41A-0350).

Lustrino, M., Keskin, M., Mattioli, M., & Kavak, O. (2012). Heterogeneous mantle sources feeding the volcanic activity of Mt. Karacadağ (SE Turkey). *Journal of Asian Earth Sciences*, *46*, 120–139. https://doi.org/10.1016/j.jseaes.2011.11.016

Ma, G. S. K., Malpas, J., Xenophontos, C., & Chan, G. H. N. (2011). Petrogenesis of latest miocene-quaternary continental intraplate volcanism along the northern Dead Sea Fault System (Al Ghab-Homs volcanic field), western Syria: Evidence for lithosphere-asthenosphere interaction. *Journal of Petrology*, *52*(2), 401–430. https://doi.org/10.1093/petrology/egq085

Mackenzie, G. D., Thybo, H., & Maguire, P. K. H. (2005). Crustal velocity structure across the Main Ethiopian Rift: Results from two-dimensional wide-angle seismic modelling. *Geophysical Journal International*, *162*(3), 994–1006. https://doi.org/10.1111/j.1365-246X.2005.02710.x

Maguire, P. K. H., Ebinger, C. J., Stuart, G. W., Mackenzie, G. D., Whaler, K. A., Kendall, J. M., et al. (2003). Geophysical project in ethiopia studies continental breakup. *Eos*, *84*(35), 3–8. https://doi.org/10.1029/2003EO350002

Mana, S., Furman, T., Turrin, B. D., Feigenson, M. D., & Swisher, C. C. (2015). Magmatic activity across the East African North Tanzanian Divergence Zone. *Journal of the Geological Society*, *172*, 368–389. https://doi.org/10.1144/jgs2014-072

Matthews, K. J., Maloney, K. T., Zahirovic, S., Williams, S. E., Seton, M., & Müller, R. D. (2016). Global plate boundary evolution and kinematics since the late Paleozoic. *Global and Planetary Change*, *146*, 226–250. https://doi.org/10.1016/j.gloplacha.2016.10.002

Mechie, J., Abu-Ayyash, K., Ben-Avraham, Z., El-Kelani, R., Mohsen, A., Rümpker, G., et al. (2005). Crustal shear velocity structure across the Dead Sea Transform from two-dimensional modelling of DESERT project explosion seismic data. *Geophysical Journal International*, *160*(3), 910–924. https://doi.org/10.1111/j.1365-246X.2005.02526.x

Mechie, J., Abu-ayyash, K., Ben-Avraham, Z., El-Kelani, R., Qabbani, I., Weber, M., et al. (2009). Crustal structure of the southern Dead Sea basin derived from project DESIRE wide-angle seismic data. *Geophysical Journal International*, *178*(1), 457–478. https://doi.org/10.1111/j.1365-246X.2009.04161.x

Van Der Meer, D. G., Spakman, W., Van Hinsbergen, D. J. J., Amaru, M. L., & Torsvik, T. H. (2010). Towards absolute plate motions constrained by lower-mantle slab remnants. *Nature Geoscience*, *3*(1), 36–40. https://doi.org/10.1038/ngeo708

Mohsen, A., Kind, R., Sobolev, S. V., & Weber, M. (2006). Thickness of the lithosphere east of the Dead Sea Transform. *Geophysical Journal International*, *167*(2), 845–852. https://doi.org/10.1111/j.1365-246X.2006.03185.x

Muller, R. D., Royer, J. Y., & Lawver, L. A. (1993). Revised plate motions relative to the hotspots from combined Atlantic and Indian Ocean hotspot tracks. *Geology*, *21*(3), 275–278. https://doi.org/10.1130/0091-7613(1993)021<0275:RPMRTT>2.3.CO;2

Nyblade, A. A., & Langston, C. A. (2002). Broadband seismic experiments probe the East African rift. *Eos*, *83*(37). https://doi.org/10.1029/2002EO000296

Nyblade, A. A., Dirks, P., & Graham, G. (2008). AfricaArray: Developing a geosciences workforce for Africa's natural resource sector. *Leading Edge*, *27*(10), 1358–1361. https://doi.org/10.3109/09638239209005451

Nyblade, A. A., Durrheim, R., Dirks, P., Graham, G., Gibson, R., & Webb, S. (2011). Geoscience Initiative develops sustainable science in Africa. *Eos*, *92*(19), 161–162. https://doi.org/10.1029/2011EO190002

Nyblade, A. A., Birt, C., Langston, C. A., Owens, T. J., & Last, R. J. (1996). Seismic experiment reveals rifting of craton in Tanzania. *Eos*, *77*(51). https://doi.org/10.1029/96EO00339

O'Neill, C., Müller, D., & Steinberger, B. (2005). On the uncertainties in hot spot reconstructions and the significance of moving hot spot reference frames. *Geochemistry, Geophysics, Geosystems*, *6*(4), Q04003.

Özdemir, Y., Karaoğlu, Ö., Tolluoğlu, A. Ü., & Güleç, N. (2006). Volcanostratigraphy and petrogenesis of the Nemrut stratovolcano (East Anatolian High Plateau): The most recent post-collisional volcanism in Turkey. *Chemical Geology*, *226*(3–4), 189–211. https://doi.org/10.1016/j.chemgeo.2005.09.020

Paul, A., Hatzfeld, D., Karabulut, H., Hatzidimitriou, P., Childs, D. ~M., Nikolova, S., et al. (2008). The SIMBAAD Experiment in W-Turkey and Greece: A Dense Seismic Network to Study the Crustal and Mantle Structures. In *AGU Fall Meeting Abstracts* (Vol. 2008, pp. T21A-1926).

Pik, R., Deniel, C., Coulon, C., Yirgu, G., & Marty, B. (1999). Isotopic and trace element signatures of Ethiopian flood basalts: Evidence for plume-lithosphere interactions. *Geochimica et Cosmochimica Acta*, *63*(15), 2263–2279. https://doi.org/10.1016/S0016-7037(99)00141-6

Pitilakis, K., Karapetrou, S., Bindi, D., Manakou, M., Petrovic, B., Roumelioti, Z., et al. (2016). Structural monitoring and earthquake early warning systems for the AHEPA hospital in Thessaloniki. *Bulletin of Earthquake Engineering*, *14*(9), 2543–2563. https://doi.org/10.1007/s10518-016-9916-5

Qaysi, S., Liu, K. H., & Gao, S. S. (2018). A database of shear-wave splitting measurements for the Arabian plate. *Seismological Research Letters*, *89*(6), 2294–2298.

https://doi.org/10.1785/0220180144

Rodgers, A., Harris, D., Ruppert, S., Lewis, J. P., O'Boyle, J., Pasyanos, M., et al. (2003). A broadband seismic deployment in Jordan. *Seismological Research Letters*, *74*(4), 374–381. https://doi.org/10.1785/gssrl.74.4.374

Rooney, T. O. (2017). The Cenozoic magmatism of East-Africa: Part I — Flood basalts and pulsed magmatism. *Lithos*, *286–287*, 264–301. https://doi.org/10.1016/j.lithos.2017.05.014

Rooney, T. O. (2020). The Cenozoic magmatism of East Africa: Part II – Rifting of the mobile belt. *Lithos*, *360–361*, 105291. https://doi.org/10.1016/j.lithos.2019.105291

Sandvol, E., Seber, D., Barazangi, M., Vernon, F. L., Mellors, R., & Al-amri, A. M. (1998). Lithospheric seismic velocity discontinuities beneath the Arabian Shield. *Geophysical Research Letters*, *25*(15), 2873–2876.

Sandvol, E., Turkelli, N., & Barazangi, M. (2003). The Eastern Turkey Seismic Experiment: The study of a young continent-continent collision. *Geophysical Research Letters*, *30*(24), 1–2. https://doi.org/10.1029/2003GL018912

Sandvol, E., Al-Damegh, K., Calvert, A., Seber, D., Barazangi, M., Mohamad, R., et al. (2001). Tomographic imaging of Lg and Sn propagation in the Middle East. *Pure and Applied Geophysics*, *158*(7), 1121–1163. https://doi.org/10.1007/978-3-0348-8262-0_3

Schettino, A., & Scotese, C. R. (2005). Apparent polar wander paths for the major continents (200 Ma to the present day): A palaeomagnetic reference frame for global plate tectonic reconstructions. *Geophysical Journal International*, *163*(2), 727–759. https://doi.org/10.1111/j.1365-246X.2005.02638.x

Schilling, J., Kingsley, R. H., Hanan, B. B., & Mccully, B. L. (1992). Nd-Sr-Pb Isotopic Variations Along the Gulf of Aden' Evidence for Afar Mantle Plume-Continental

Lithosphere Interactio. *Journal of Geophysical Research: Solid Earth*, *97*, 927–966.

Sebai, A., Zumbo, V., Féraud, G., Bertrand, H., Hussain, A. G., Giannérini, G., & Campredon, R. (1991). 40Ar39Ar dating of alkaline and tholeiitic magmatism of Saudi Arabia related to the early Red Sea Rifting. *Earth and Planetary Science Letters*, *104*(2–4), 473–487. https://doi.org/10.1016/0012-821X(91)90223-5

Sebai, A., Stutzmann, E., Montagner, J. P., Sicilia, D., & Beucler, E. (2006). Anisotropic structure of the African upper mantle from Rayleigh and Love wave tomography. *Physics of the Earth and Planetary Interiors*, *155*(1–2), 48–62. https://doi.org/10.1016/j.pepi.2005.09.009

Seton, M., Müller, R. D., Zahirovic, S., Gaina, C., Torsvik, T., Shephard, G., et al. (2012). Global continental and ocean basin reconstructions since 200Ma. *Earth-Science Reviews*, *113*(3–4), 212–270. https://doi.org/10.1016/j.earscirev.2012.03.002

Silver, P., Mainprice, D., Ismaïl, W., Tommasi, A., Silver, P., Mainprice, D., et al. (2016). Mantle structural geology from seismic anisotropy. *The Geochemical Society. Mantle Petrology: Field Observations and High Pressure Experimentations: A Tribute to Francis R. (Joe) Boyd, 6, 1999.*

Simmons, N. A., Myers, S. C., Johannesson, G., & Matzel, E. (2012). LLNL-G3Dv3: Global P wave tomography model for improved regional and teleseismic travel time prediction. *Journal of Geophysical Research: Solid Earth*, *117*(10), B10302.

Stab, M., Bellahsen, N., Pik, R., Quidelleur, X., Ayalew, D., & Leroy, S. (2016). Modes of rifting in magma-rich settings: Tectono-magmatic evolution of Central Afar. *Tectonics*, *35*(1), 2–38. https://doi.org/10.1002/2015TC003893

Stuart, G., Kendall, M., Bastow, I., Ayele, A., Ebinger, C., Maguire, P., & Fowler, M. (2002).

The EAGLE Broadband Seismic Experiment - A Study of Continental Rifting in the Ethiopia. In *AGU Fall Meeting Abstracts* (Vol. 2002, pp. T11D-1289).

Torsvik, T. H., Steinberger, B., Cocks, L. R. M., & Burke, K. (2008). Longitude: Linking Earth's ancient surface to its deep interior. *Earth and Planetary Science Letters*, *276*(3–4), 273–282. https://doi.org/10.1016/j.epsl.2008.09.026

Torsvik, T. H., Steinberger, B., Shephard, G. E., Doubrovine, P. V., Gaina, C., Domeier, M., et al. (2019). Pacific-Panthalassic Reconstructions: Overview, Errata and the Way Forward. *Geochemistry, Geophysics, Geosystems*, *20*(7), 3659–3689. https://doi.org/10.1029/2019GC008402

Torsvik, T. H., Van der Voo, R., Preeden, U., Mac Niocaill, C., Steinberger, B., Doubrovine, P. V., et al. (2012). Phanerozoic Polar Wander, Palaeogeography and Dynamics. *Earth-Science Reviews*, *114*(3–4), 325–368. https://doi.org/10.1016/j.earscirev.2012.06.007

Tumanova, N., Kakhoberashvili, S., Omarashvili, V., Tserodze, M., & Akubardia, D. (2016). National Seismic Network of Georgia. In *AGU Fall Meeting Abstracts* (Vol. 2016, pp. S11D-2498).

Weinstein, Y., & Garfunkel, Z. (2014). The Dead Sea Transform and the Volcanism in Northwestern Arabia. In *Dead Sea Transform Fault System: Reviews* (Vol. 6, pp. 91–108).